Nonlinear static analysis of metamaterial structures based on the Kagome lattice using beam finite elements and component-wise approach

International Journal of Solids and Structures 318 (2025) 113387

Contents lists available at ScienceDirect

International Journal of Solids and Structures

journal homepage: www.elsevier.com/locate/ijsolstr

Nonlinear static analysis of metamaterial structures based on the Kagome lattice using beam finite elements and component-wise approach

R. Augello [a,*,1], E. Carrera [a,2], W.Q. Chen [b,3], B. Wu [b,4], Y.Z. Wang [b,5]

[a] Mul^2 Group, Department of Mechanical and Aerospace Engineering, Politecnico di Torino, Corso Duca degli Abruzzi 24, 10129 Torino, Italy
[b] Key Laboratory of Soft Machines and Smart Devices of Zhejiang Province, & Department of Engineering Mechanics, & Soft Matter Research Center., Zhejiang University, Hangzhou 310027, China

ARTICLE INFO

Keywords:
Metamaterials
Kagome lattice
Finite element method
Carrera Unified Formulation
3D metastructure

ABSTRACT

This work numerically investigates the mechanical behavior of metamaterial structures inspired by the Kagome lattice mechanism using the Carrera Unified Formulation (CUF). The proposed numerical model employs enhanced one-dimensional finite elements with three-dimensional capabilities, enabling precise predictions of deformation patterns and stress–strain responses under various loading conditions. With CUF, any three-dimensional effects can be captured, allowing for the analysis of the width direction of these metamaterial structures, potentially accounting for varying geometric properties. The model's robustness is demonstrated through its ability to capture critical phenomena such as buckling, post-buckling behavior, and rigid-body rotations of lattice triangles, which are hallmarks of the Kagome lattice's unique mechanical properties. The introduction of stiffer hinges highlights the potential for tailoring mechanical responses to meet specific design requirements, such as enhanced load-carrying capacity and optimized energy absorption. This study demonstrates the versatility of Kagome lattice-based metamaterials and lays the groundwork for future research, including the analysis of 3D Kagome-lattice metamaterials facilitated to the proposed numerical model.

1. Introduction

Metamaterials are artificially engineered materials designed to exhibit unique and extraordinary mechanical, thermal, or electromagnetic properties that are not commonly found in natural materials. These structures derive their properties primarily from their geometry rather than their material composition, allowing for precise control over various physical phenomena. Their ability to manipulate wave propagation, stress distribution, and energy absorption makes metamaterials invaluable in numerous fields, including aerospace, civil engineering, and biomedical applications. For example, metamaterials have been employed in the design of vibration isolators (Al Rifaie et al., 2022), impact absorbers (Huang et al., 2012), and devices for wave steering and energy harvesting (Chen et al., 2014). The importance of metamaterials lies in their ability to provide solutions to longstanding challenges, such as creating ultra-lightweight structures with high stiffness or designing materials with negative Poisson's ratios for improved flexibility (Babaee et al., 2013). This versatility has driven the rapid adoption of metamaterials in cutting-edge technologies and industrial applications.

Among the vast list of possible designs of metamaterials, the Kagome lattice, a two-dimensional arrangement of interconnected equilateral triangles, is renowned for its unique combination of mechanical and geometric properties. Derived from a traditional Japanese basket-weaving pattern, this structure has been widely studied for its ability to achieve a balance of high stiffness, low weight, and mechanical efficiency (Wang et al., 2021). The intrinsic geometric symmetry of the Kagome lattice results in near-isotropic properties, making it particularly well-suited for applications requiring uniform mechanical performance in multiple

* Corresponding author.
E-mail addresses: riccardo.augello@polito.it (R. Augello), erasmo.carrera@polito.it (E. Carrera), chenwq@zju.edu.cn (W.Q. Chen), bin.wu@zju.edu.cn (B. Wu), yzwangzju@gmail.com (Y.Z. Wang).
[1] Postdoc.
[2] Full Professor of Aeronautics and Astronautics.
[3] Full Professor.
[4] Tenure-track Professor.
[5] Researcher.

https://doi.org/10.1016/j.ijsolstr.2025.113387
Received 24 January 2025; Received in revised form 21 March 2025; Accepted 9 April 2025
Available online 6 May 2025

directions (Bauer et al., 2017). One of the defining features of Kagome lattices is their capability to sustain large deformations without material failure. This is achieved through the rigid-body rotations of their triangular units, which redistribute loads and allow for energy dissipation. Such behavior makes Kagome lattices ideal candidates for applications in energy absorption, impact mitigation, and morphing structures. For example, in crashworthiness and protective equipment, these lattices can dissipate energy efficiently while maintaining structural integrity (Hou et al., 2023). Additionally, their periodic arrangement and inherent stiffness allow for tailored mechanical responses, including negative Poisson's ratios and tunable stiffness, further expanding their potential applications in advanced structural systems (Li et al., 2024). Beyond their mechanical properties, Kagome lattices have also been employed in wave propagation studies. Their periodic geometry enables the design of acoustic and elastic metamaterials with tunable band gaps, which can manipulate sound and vibration at specific frequencies (Wu et al., 2015; Nassar et al., 2020; Li and Kohn, 2023). This functionality has led to their integration into vibration isolators (An et al., 2023b,a) and waveguiding devices (Ablowitz and Cole, 2019), highlighting their versatility across different engineering domains.

Accurate numerical modeling of Kagome lattices is critical for understanding and predicting their complex mechanical behavior, as well as for reducing the number of experimental tests that can be expensive and time-consuming. Traditional Finite Element Methods (FEM) are widely used in structural analysis due to their general applicability and well-established frameworks. However, modeling the intricate geometry and unique deformation mechanisms of Kagome lattices often poses significant challenges for conventional FEM. The rigid-body rotations of the triangular units, large deformations, and localized stress concentrations require a high level of precision, which often necessitates extremely fine meshing. This, in turn, results in increased computational costs and longer simulation times, particularly for large-scale lattices (Vigliotti and Pasini, 2012; Nikolić et al., 2018). To address these limitations, researchers have explored advanced numerical techniques tailored to the specific needs of lattice structures. Enriched finite element methods, for instance, incorporate additional degrees of freedom to capture local deformations more accurately without significantly increasing computational demands. Isogeometric analysis has also been applied to Kagome lattices (Maurin et al., 2019; Wang et al., 2017, 2018), making use of the smoothness of spline-based functions to enhance accuracy and convergence rates. Similarly, techniques such as homogenization (Vlădulescu and Constantinescu, 2020; Somnic and Jo, 2022; Arabnejad and Pasini, 2013) and reduced-order modeling (Lin et al., 2021; McBane and Choi, 2021) allow for the efficient simulation of repetitive lattice structures by simplifying their geometric representation while preserving essential mechanical characteristics. Other approaches include the use of multi-scale methods (Liu et al., 2021; Damanpack et al., 2019; Zhang et al., 2010), where the global structural behavior of the structure is coupled with detailed local analyses to capture both macro-scale performance and micro-scale deformations. These techniques are particularly beneficial for studying the hierarchical nature of Kagome lattices, where the interplay between global and local behaviors defines the overall mechanical response. The integration of these advanced modeling approaches ensures the efficient and accurate analysis of Kagome lattices, enabling their use in real-world applications and facilitating their optimization for specific design requirements. By employing advanced numerical methods (Chen et al., 2018; Tankasala et al., 2017; Nelissen et al., 2019), researchers can overcome many challenges associated with traditional FEM. However, a common characteristic of such methodologies is their reliance on simplifying assumptions. As a result, specific local phenomena or the extension to fully three-dimensional (3D) problems remain undetectable. Therefore, the development of a reliable numerical model capable of accurately predicting the behavior of lattice metamaterial structures could represent a crucial breakthrough in the analysis of these systems.

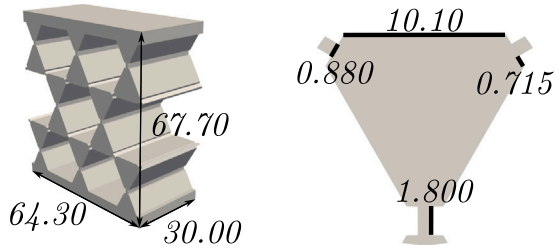

Fig. 1. Considered metamaterial structure based on Kagome mechanism. Geometric characteristics are taken from Li et al. (2024). Dimensions are expressed in mm.

This work presents a solution that combines FEM with the Carrera Unified Formulation (CUF) (Carrera et al., 2011, 2014). CUF facilitates the development of one-dimensional (1D) Finite Elements (FEs) with enhanced modeling capabilities. Specifically, the formulation extends the standard FE nodes through the use of expansion functions, enabling the detection and representation of cross-sectional deformations (Cinefra et al., 2021). By employing Lagrange elements as expansion functions, the methodology can accommodate arbitrarily complex geometries, making it particularly suitable for structures with intricate shapes. This flexibility is especially advantageous for the analysis of metamaterials, where the geometric complexity often poses significant modeling challenges. The proposed framework leverages these expansion functions to accurately capture the behavior of metamaterials, including their nonlinear and anisotropic characteristics (Augello and Carrera, 2024; Carrera et al., 2024). Nonlinear governing equations are systematically addressed by formulating the tangent stiffness matrix, which remains independent of the specific type of expansion functions employed. This independence ensures a high degree of adaptability and computational efficiency. CUF has been used for several engineering application, including the analysis of rotor blades (Filippi et al., 2018), aircraft wings (Carrera and Pagani, 2016) and spacecraft (Augello et al., 2023b; Augello and Pellegrino, 2025). In addition, CUF has demonstrated exceptional performance in addressing geometrically nonlinear problems (Pagani et al., 2019; Carrera et al., 2021). In this work, the formulation is further extended to enable the analysis of metamaterials structured based on Kagome lattice configurations.

2. One-dimensional beam finite element for the modeling of metamaterial structures

The metamaterial based on the Kagome mechanism is shown in Fig. 1. The geometric properties of the analyzed metamaterial are taken from Li et al. (2024). In this work, CUF is used to construct the numerical model of this structure. The process is depicted in Fig. 2.

The 1D beam model uses the x and z coordinates for the cross-sectional domain, while y denote the axis direction. The 3D displacement field can be written as

$$\mathbf{u}(x,y,z) = \{u_x \quad u_y \quad u_z\}^{\mathrm{T}} \tag{1}$$

where T is the transpose operator. Eq. (1) of the 1D metamaterial structure is formulated within the framework of CUF, and it can be expressed as follows

$$\begin{aligned} \mathbf{u}(x,y,z) &= F_\tau(x,z)\mathbf{u}_\tau(y), \qquad \tau = 1,2,\dots,M \\ \delta\mathbf{u}(x,y,z) &= F_s(x,z)\delta\mathbf{u}_s(y), \qquad s = 1,2,\dots,M \end{aligned} \tag{2}$$

It is clear that each theory can be easily obtained from Eq. (2) by using polynomials of different orders as F_τ and F_s. In this work, Lagrange polynomials are employed. The cross-section is approximated with a pattern of Lagrange Points (LPs), which are divided into opportune sub-domains. The 3D displacement field is, then, a result of the interpolation of the displacements calculated at the LPs. The degree of the

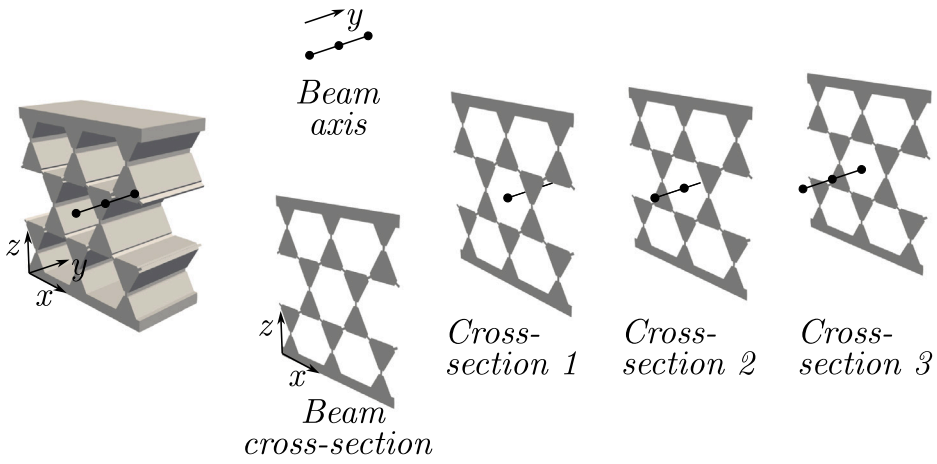

Fig. 2. Carrera unified formulation applied to the metamaterial structure for constructing the mathematical model.

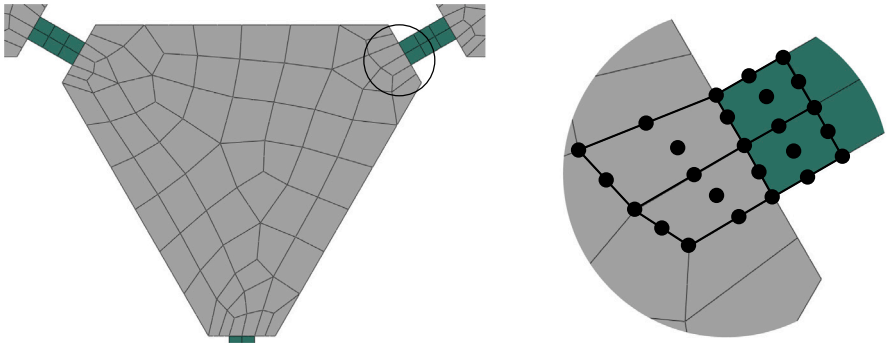

Fig. 3. Connection between rigid triangles and elastic hinges modeled using Lagrange elements.

interpolation is defined by the number of the employed LPs. Specifically, 4 LPs (L4) ensure a bilinear interpolation of the isoparametric formulation, 9 LPs (L9) a quadratic one and 16 LPs (L16) a cubic. The number of DOFs equals the sum of the displacements for each LP. For an L9, the interpolation functions are:

$$\begin{aligned} F_\tau &= \frac{1}{4}(r^2 + rr_\tau)(s^2 + ss_\tau) && \tau = 1,3,5,7 \\ F_\tau &= \frac{1}{2}s_\tau^2(s^2 - ss_\tau)(1-r^2) + \frac{1}{2}r_\tau^2(r^2 - rr_\tau)(1-s^2) && \tau = 2,4,6,8 \\ F_\tau &= (1-r^2)(1-s^2) && \tau = 9 \end{aligned} \tag{3}$$

where r and s vary from -1 to $+1$, whereas r_τ and s_τ are the coordinates of the nine LPs whose locations are defined in the natural coordinate frame. For more details, interested readers are referred to Carrera et al. (2014). In this work, L9 elements are used and Fig. 3 shows the connection between the rigid triangles and the elastic hinges modeled using Lagrange elements. The displacement field of an L9 is therefore

$$\begin{aligned} u_x(x,y,z) &= F_1(x,z)u_{x_1}(y) + F_2(x,z)u_{x_2}(y) + \ldots + F_9(x,z)u_{x_9}(y) \\ u_y(x,y,z) &= F_1(x,z)u_{y_1}(y) + F_2(x,z)u_{y_2}(y) + \ldots + F_9(x,z)u_{y_9}(y) \\ u_z(x,y,z) &= F_1(x,z)u_{z_1}(y) + F_2(x,z)u_{z_2}(y) + \ldots + F_9(x,z)u_{z_9}(y) \end{aligned} \tag{4}$$

in which u_{x_1}, …, u_{z_9} represent the displacement components of each of the nine LPs.

The *generalized* displacements $\mathbf{u}_\tau$ and the *generalized* variations $\delta\mathbf{u}_s$ in Eq. (2) are expanded using the Finite Element Method (FEM) as follows

$$\begin{aligned} \mathbf{u}_\tau(y) &= N_i(y)\mathbf{q}_{\tau i}, \qquad i = 1,2,\ldots.,N_n \\ \delta\mathbf{u}_s(y) &= N_j(y)\mathbf{q}_{sj}, \qquad j = 1,2,\ldots.,N_n \end{aligned} \tag{5}$$

where N_n is the number of the nodes for each Finite Element (FE) and N_i and N_j are the shape functions, $\mathbf{q}_{\tau i}$ and $\mathbf{q}_{sj}$ are the vectors of the FE nodal parameters, expressed as

$$\begin{aligned} \mathbf{q}_{\tau i} &= \left\{ u_{x_{\tau i}} \; u_{y_{\tau i}} \; u_{z_{\tau i}} \right\}^T \\ \delta\mathbf{q}_{sj} &= \left\{ \delta u_{x_{sj}} \; \delta u_{y_{sj}} \; \delta u_{z_{sj}} \right\}^T \end{aligned} \tag{6}$$

The shape functions N_i and N_j are not reported here but can be found in many reference texts, for instance, in Bathe (Bathe, 2006). In this work, the metamaterial structure based on the Kagome mechanism is modeled using a single three-node quadratic element (B3).

3. Metamaterial structures with varying cross-section geometry

In the previous example, the primary goal is to model a metamaterial based on Kagome lattice geometry with a constant cross-section along the length of the beam. Thus, the structural deformation is confined to the 2D cross-sectional plane. In contrast, the example presented in this section explores a metamaterial structure whose geometry and triangular pattern vary in the transverse direction (the axis of our 1D FE model). This variation is achieved through the capabilities of CUF, which allow the cross-sectional geometry to change along the length of the metamaterial, thereby enabling the modeling of more complex 3D structures. Fig. 4 depicts the structure with non-uniform cross-sections that will be analyzed, serving as an illustration of the potential of this approach. In particular, three different cross-section geometries alternate to build the mathematical model of the entire structure, with the dimensions reported in Fig. 5. In this context, the yellow components correspond to the rigid triangles, the red components to the elastic hinges, and the green domains represent the loading and constraining areas. Finally, Fig. 6 shows the construction process of the numerical model. The first B3 FE is modeled with cross-section 1, and the same is applied to the B3 elements in the middle and at the end of the structure. The two inner four-node elements

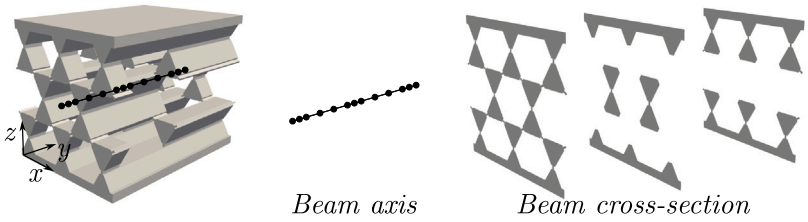

Fig. 4. Using the Carrera Unified Formulation, a mathematical model is constructed for the metamaterial structure by incorporating multiple cross-sectional geometries. The beam cross-sections alternate along the structure's length to capture the overall geometry of the system.

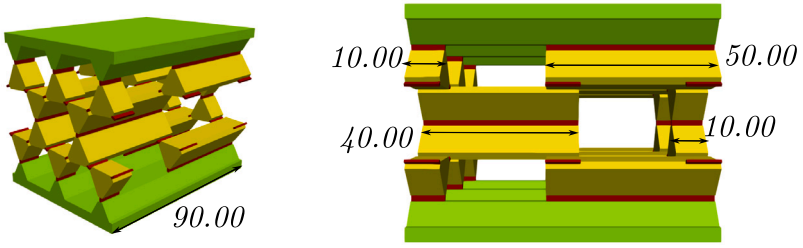

Fig. 5. Geometric properties of the metamaterial structure with different cross-sections. The dimensions are expressed in mm. The yellow components correspond to the rigid triangles, the red components to the elastic hinges and the green domains are the loading and constraining areas. The dimensions not shown are the same as those in Fig. 1.

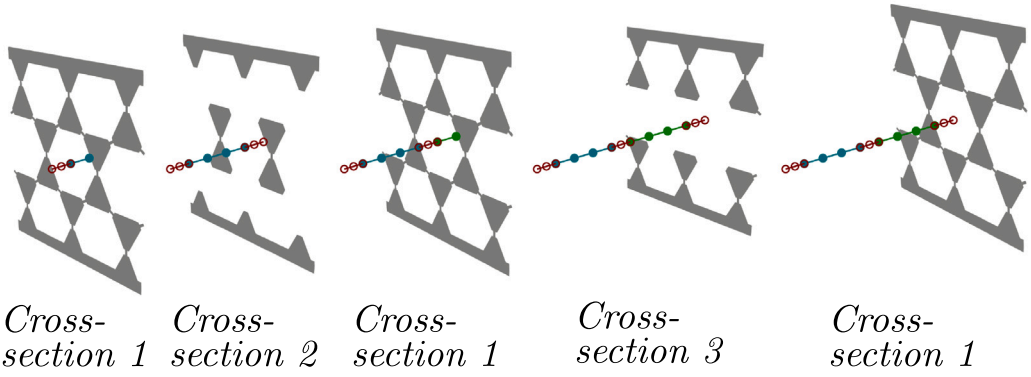

Fig. 6. Different cross-sections of the metamaterial structure shown in Fig. 4.

with cubic interpolation (B4) are modeled with cross-section 2 and 3, respectively.

4. Governing equations of metamaterial structures

In this paper, the vectorial form of the stress, $\boldsymbol{\sigma}$, and strain, $\boldsymbol{\epsilon}$, components are introduced as

$$\boldsymbol{\sigma} = \{\sigma_{xx} \;\; \sigma_{yy} \;\; \sigma_{zz} \;\; \sigma_{xz} \;\; \sigma_{yz} \;\; \sigma_{xy}\}^{\mathrm{T}}, \quad \boldsymbol{\epsilon} = \{\epsilon_{xx} \;\; \epsilon_{yy} \;\; \epsilon_{zz} \;\; \epsilon_{xz} \;\; \epsilon_{yz} \;\; \epsilon_{xy}\}^{\mathrm{T}} \tag{7}$$

As far as the strain field is concerned, the Green–Lagrange nonlinear strain components are

$$\boldsymbol{\epsilon} = \boldsymbol{\epsilon}_l + \boldsymbol{\epsilon}_{nl} = (\mathbf{b}_l + \mathbf{b}_{nl})\mathbf{u}, \tag{8}$$

where the 6×3 linear and nonlinear differential operators $\mathbf{b}_l$ and $\mathbf{b}_{nl}$ are given by:

$$\mathbf{b}_l = \begin{bmatrix} \partial_x & 0 & 0 \\ 0 & \partial_y & 0 \\ 0 & 0 & \partial_z \\ \partial_z & 0 & \partial_x \\ 0 & \partial_z & \partial_y \\ \partial_y & \partial_x & 0 \end{bmatrix}, \quad \mathbf{b}_{nl} = \begin{bmatrix} \frac{1}{2}(\partial_x)^2 & \frac{1}{2}(\partial_x)^2 & \frac{1}{2}(\partial_x)^2 \\ \frac{1}{2}(\partial_y)^2 & \frac{1}{2}(\partial_y)^2 & \frac{1}{2}(\partial_y)^2 \\ \frac{1}{2}(\partial_z)^2 & \frac{1}{2}(\partial_z)^2 & \frac{1}{2}(\partial_z)^2 \\ \partial_x\partial_z & \partial_x\partial_z & \partial_x\partial_z \\ \partial_y\partial_z & \partial_y\partial_z & \partial_y\partial_z \\ \partial_x\partial_y & \partial_x\partial_y & \partial_x\partial_y \end{bmatrix} \tag{9}$$

in which $\partial_\alpha = \partial(\cdot)/\partial\alpha$, $\partial_\beta = \partial(\cdot)/\partial\beta$, and $\partial_z = \partial(\cdot)/\partial z$.

Linear elastic isotropic materials are considered in this work and the constitutive relation reads as

$$\boldsymbol{\sigma} = \mathbf{C}\,\boldsymbol{\epsilon}, \tag{10}$$

where $\mathbf{C}$ is the material elastic matrix, whose explicit form can be found in Bathe (2006), Hughes (2012). In this work, the principle of virtual work is recalled for the derivation of the FE governing equations, which, for a generic structure, can be expressed as:

$$\delta L_{\text{int}} = \delta L_{\text{ext}} \tag{11}$$

where δL_{int} is the virtual variation of the work of the internal loads (i.e. the strain energy) and δL_{ext} is the virtual variation of the work of the external loads.

The first term of Eq. (11) can be written as:

$$\delta L_{\text{int}} = \int_V \delta\boldsymbol{\epsilon}^T \boldsymbol{\sigma}\, \mathrm{d}V \tag{12}$$

where V is the volume of the body. Introducing the geometrical (Eq. (8)) and constitutive relations (Eq. (10)) into Eq. (12), it takes the following form:

$$\delta L_{\text{int}} = \delta \mathbf{q}_{sj}^T \mathbf{K}_S^{ij\tau s} \mathbf{q}_{\tau i} \tag{13}$$

The argument of the integral in Eq. (13) represents the so-called secant stiffness matrix $\mathbf{K}_S^{ij\tau s}$. The complete form of the secant stiffness matrix

$\mathbf{K}_S^{ij\tau s}$ is omitted here for the sake of brevity, but can be found in Pagani and Carrera (2018), Carrera et al. (2018).

The right-hand term of Eq. (11), omitting some mathematical steps that can be found in Carrera et al. (2011), can be written as:

$$\delta L_{\text{ext}} = \delta \mathbf{q}_{sj}^T \, \mathbf{p}_{sj} \tag{14}$$

so that Eq. (11) becomes:

$$\mathbf{K}_S^{ij\tau s} \mathbf{q}_{\tau i} - \mathbf{p}_{sj} = \mathbf{0} \tag{15}$$

Eq. (15) can be arbitrarily expanded to achieve any desired theory, ranging from low- to high-order ones, by choosing the values for $\tau, s = 1, 2, \dots, M$ and $i, j = 1, 2, \dots, N_n$, resulting in:

$$\mathbf{K}_S \, \mathbf{q} - \mathbf{p} = \mathbf{0} \tag{16}$$

where $\mathbf{K}_S$, $\mathbf{q}$, and $\mathbf{p}$ are the global, assembled FE arrays of the final structure.

Eq. (16) represents a geometrically nonlinear system and it is typically computed adopting a linearization technique. In this paper, the employed scheme is the Newton–Raphson method, according to which the nonlinear governing equations are expressed as

$$\boldsymbol{\varphi}_{res} \equiv \mathbf{K}_S \, \mathbf{q} - \mathbf{p} = \mathbf{0} \tag{17}$$

where the *residual nodal forces* vector is expressed in $\boldsymbol{\varphi}_{res}$. One can use a known solution $(\mathbf{q}, \mathbf{p})$ to linearize Eq. (17) by expanding $\boldsymbol{\varphi}_{res}$ in a Taylor series. Therefore,

$$\boldsymbol{\varphi}_{res}(\mathbf{q} + \delta\mathbf{q}, \mathbf{p} + \delta\mathbf{p}) = \boldsymbol{\varphi}_{res}(\mathbf{q}, \mathbf{p}) + \frac{\partial \boldsymbol{\varphi}_{res}}{\partial \mathbf{q}} \, \delta\mathbf{q} + \frac{\partial \boldsymbol{\varphi}_{res}}{\partial \mathbf{p}} \, \delta\lambda \, \mathbf{p}_{ref} = \mathbf{0} \tag{18}$$

where $\dfrac{\partial \boldsymbol{\varphi}_{res}}{\partial \mathbf{q}} = \mathbf{K}_T$ represents the *tangent* stiffness matrix. The external load is assumed to change directly with the vector of the reference loadings $\mathbf{p}_{ref}$, with a variation rate expressed by λ, defined as the load-scaling parameter, i.e. $\mathbf{p} = \lambda \mathbf{p}_{ref}$. Since λ is a variable, an additional constraint equation is required, which is given by a relation constraining both $\delta\mathbf{q}$ and $\delta\lambda$. Finally, one has

$$\begin{cases} \mathbf{K}_T \, \delta\mathbf{q} = \delta\lambda \, \mathbf{p}_{ref} - \boldsymbol{\varphi}_{res} \\ c(\delta\mathbf{q}, \delta\lambda) = \mathbf{0} \end{cases} \tag{19}$$

In this work, a path-following technique is adopted as the constraint equation. Specifically, an arc-length method is utilized in this work, as described by Crisfield (Crisfield, 1981, 1983) and Carrera (Carrera, 1994). It is important to underline that $\mathbf{K}_T$ is derived from the linearization of the equilibrium equations (Zienkiewicz and Taylor, 2005). This corresponds to the linearization of the virtual variation of the work made by internal forces in the case of conservative systems, as follows

$$\delta(\delta L_{\text{int}}) = \int_{\text{V}} \delta \left(\delta \boldsymbol{\epsilon}^T \boldsymbol{\sigma} \right) \, \text{dV} = \delta \mathbf{q}_{\tau i}^T \mathbf{K}_T^{ij\tau s} \delta \mathbf{q}_{sj} \tag{20}$$

where $\mathbf{K}_T^{ij\tau s}$ represents the 3×3 *fundamental nucleus*, which serves as the basic building block for constructing the total tangent stiffness matrix.

5. Numerical results and discussion

This section presents the numerical results obtained from the analysis. The structures depicted in Figs. 1 and 4 are evaluated under specific boundary conditions, as illustrated in Fig. 7. Both structures are clamped at their base, providing a fixed boundary condition, and subjected to a compressive force applied to their top surfaces. The results are expressed as a σ vs. ϵ curve, where σ is calculated as the applied force F divided by the area over which the force is applied, and ϵ is determined as the ratio of the vertical displacement of the top plate to the initial height of the structure, which is 67.60 mm for both configurations. Due to the nature of the structure, incorporating a symmetry-breaking parameter in the numerical model is necessary to accurately capture the post-buckling behavior. In some instances, this parameter is provided in the reference paper, for example, through the initial rotation condition of the rigid triangles (Sections 5.1.1 and 5.5) or by imposing stiffer hinges (Section 5.4). In all other cases, a small perturbation is introduced by rotating the rigid triangles to achieve the desired configuration.

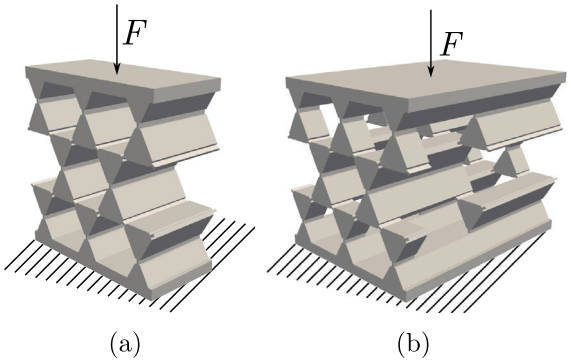

Fig. 7. Applied loading and boundary conditions.

5.1. Metamaterial structure based on Kagome mechanism

A preliminary convergence analysis was conducted to identify a reliable numerical model for subsequent simulations. Three different models, with 16,092, 30,600, and 38,952 DOF, respectively, were examined. The results of the static analysis are presented in Fig. 8. The model with 30,600 DOF can be considered as a converged model and will therefore be used for all the subsequent analyses. The same result is compared in Fig. 9 with the reference experimental solution reported in Li et al. (2024). In the reference study, it is stated that the soft hinges are composed of silicone rubber, while the stiff triangular elements are made of polylactic acid. However, their specific material properties were not provided. In the present study, isotropic material properties are assumed for both components to approximate their behavior. For the stiff triangular elements, the material is modeled with a Young's modulus of $E = 2.35$ GPa and a Poisson's ratio of $\nu = 0.375$. For the soft hinges, the assumed material properties are $E = 0.14$ GPa and $\nu = 0.480$. These material properties were derived by averaging the reported values of silicone rubber and polylactic acid from the literature, then suitably adjusted them to best align with the experimental data reported in the reference paper. Moreover, a linear elastic material model is considered in this paper for the silicon rubber and the polylactic acid.

The numerical results demonstrate a high degree of accuracy when compared to the reference solution, particularly in the low-to-moderate stress range. However, a noticeable divergence occurs as the applied stress increases significantly, likely due to differences in the modeling assumptions of the materials in the reference work, where nonlinearity is taken into consideration through the nonlinear torsional springs. Fig. 9 also illustrates the deformed configuration at $\epsilon = 0.05$, highlighting the capability of the numerical model to reliably predict the deformed shape. Additional deformed configurations at $\epsilon = 0.003$, $\epsilon = 0.010$, and $\epsilon = 0.030$ are presented in Fig. 10, further validating the consistency of the numerical model in capturing the mechanical response and deformation patterns across varying strain levels. These results underline the robustness of the numerical approach and reinforce confidence in its application to similar structures.

5.1.1. Metamaterial structure based on Kagome mechanism with initial condition

A second analysis, inspired by the reference study, is conducted by initially rotating the triangular elements by an angle of $\theta = 1.5°$, as illustrated in Fig. 11. This modification aims to assess the impact of geometric preconditioning on the structural response. The resulting σ

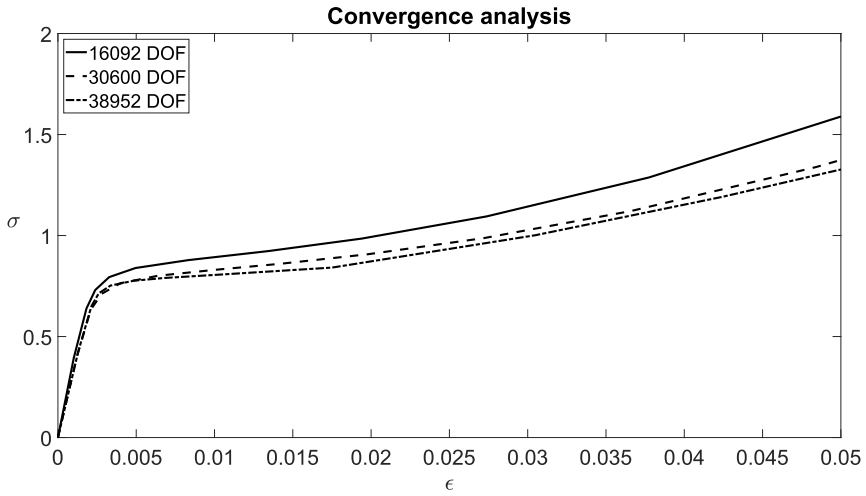

Fig. 8. Results of the convergence analysis for the metamaterial structure shown in Fig. 7(a). σ is calculated as the applied force F divided by the area over which the force is applied, while ϵ is determined as the ratio of the vertical displacement of the top plate to the initial structure height (67.60 mm).

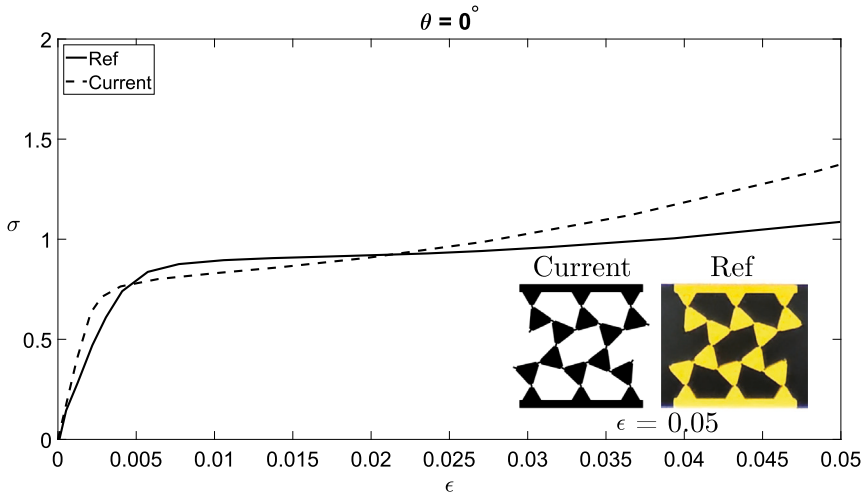

Fig. 9. Evolution of σ vs. ϵ for the metamaterial structure shown in Fig. 7(a). Ref results are taken from Li et al. (2024). σ is calculated as the applied force F divided by the area over which the force is applied, while ϵ is determined as the ratio of the vertical displacement of the top plate to the initial structure height (67.60 mm).

vs. ϵ curve for this configuration is presented in Fig. 12. Compared to the previous case (without initial rotation), this analysis exhibits greater accuracy in capturing the reference solution, particularly in the moderate and high-stress regions. This improvement suggests that the initial rotation enhances the ability of the numerical model to align with the deformation characteristics observed in the reference. The reliability of the numerical approach is further supported by examining the deformed shapes at various strain levels. The deformed configuration at $\epsilon = 0.05$ is shown in Fig. 12, closely matching the expected deformation patterns. Additionally, intermediate configurations at $\epsilon = 0.003$, $\epsilon = 0.010$, and $\epsilon = 0.030$ are detailed in Fig. 13, providing a comprehensive view of the structural evolution throughout the loading process. These results highlight the significance of initial geometric conditions in influencing the mechanical response. The improved accuracy underscores the robustness of the numerical model in predicting both global and local deformation behavior.

5.2. Metamaterial structure with a stiffer hinge

The same structural configuration analyzed previously is revisited with a modification that introduces a stiffer hinge at the bottom, as illustrated in Fig. 14. This hinge is reinforced by increasing its stiffness through the multiplication of its Young's modulus by a factor of 10^3. This modification aims to evaluate the impact of a significantly stiffer hinge on the overall structural response. The same loading conditions and boundary constraints applied in the earlier analysis are maintained for this case, allowing for a direct examination of how the enhanced hinge stiffness influences the σ vs. ϵ relationship. The resulting σ vs. ϵ behavior is depicted in Fig. 14, highlighting the altered response due to the increased hinge stiffness. The comparison with results from Fig. 10 underscores the significant role of hinge stiffness in governing the mechanical behavior of the structure. The results demonstrate a high level of overall accuracy, indicating the model's effectiveness in capturing the essential mechanical behavior of the structure. However, certain discrepancies become evident at moderate and large strain levels. These deviations are likely attributable to the material modeling of the hinges, which in this study is assumed to exhibit linear elastic behavior. At higher strain levels, the linear material assumption may no longer be valid, leading to the observed differences.

Despite these limitations, the deformed shape of the structure is captured with remarkable precision by the current model. This is illustrated in Fig. 15, which presents the deformed configurations at $\epsilon = 0.05$. The figure clearly showcases the model's capability to replicate both the geometry and the overall deformation pattern of the structure under the applied strain.

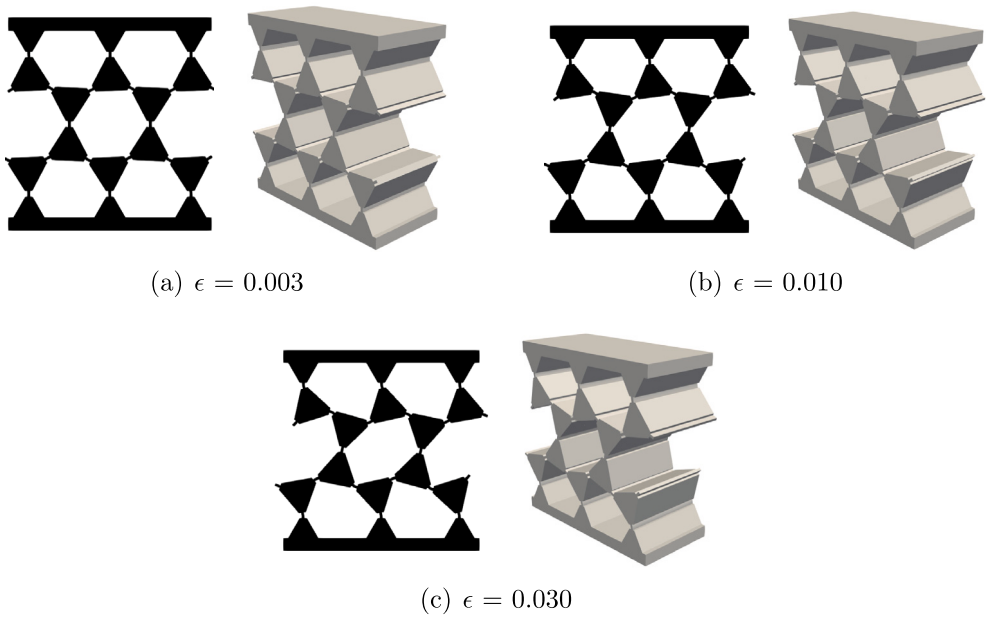

Fig. 10. Snapshots of the metamaterial structure shown in Fig. 7(a), with a cross-sectional view taken at $y = 0$ mm.

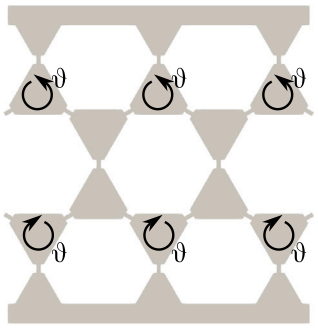

Fig. 11. Initial condition for the second analysis with $\theta = 1.5°$.

5.3. Beam-like metamaterial structure

The next case study focuses on a beam-like metamaterial structure constructed using the same Kagome lattice configuration as in the previous analyses. The structure, illustrated in Fig. 16, consists of a grid formed by 7 × 26 triangles and two stiff horizontal strips. The same boundary conditions are applied as in prior studies, that is the structure is subjected to uniaxial compression on one side, while the opposite side is clamped. The numerical model for this case involves a total of 220,761 degrees of freedom. The results of the analysis, presented in Fig. 17, depict the evolution of the σ vs. ϵ relationship. The proposed model demonstrates a high degree of reliability in capturing both the buckling and post-buckling behavior of the structure, closely matching the reference solution. This agreement validates the model's effectiveness in simulating the complex mechanical responses inherent to beam-like metamaterial structures. Further evidence of the model's accuracy is provided by examining the deformed configurations at $\epsilon = 0.04$, as shown in Fig. 18. The deformations are virtually identical to the reference solution, showcasing the model's capability in replicating both the macroscopic buckling patterns and the localized rigid rotation of the triangular elements. The rigid-body rotation of the triangles, a key feature of the Kagome lattice under deformation, is particularly well captured, emphasizing the suitability of the model for such analyses.

5.4. Beam-like metamaterial structure with stiffer hinges

Finally, an analysis is conducted on the same beam-like metamaterial structure, but with the addition of stiffer hinges to investigate their influence on the structural behavior. The locations of the hinges with stiffer material properties are highlighted in Fig. 19, where the modified configuration is illustrated. These stiffer hinges are designed to enhance localized rigidity, with their material properties adjusted to provide a significantly higher stiffness compared to the original hinges, as for the case shown in Fig. 14. The stress–strain σ vs. ϵ response for this modified structure is also presented in Fig. 19. The results demonstrate the proposed model's high level of accuracy in predicting the mechanical behavior, as evidenced by the close agreement between the numerical solution and the reference data. This validation underscores the robustness of the modeling approach. Further validation is provided by examining the deformed shapes at $\epsilon = 0.04$, as shown in Fig. 20. The comparison of the deformed configurations reveals that the proposed model captures the key features of the deformation with remarkable precision. Notably, the introduction of stiffer hinges alters the deformation pattern, creating localized areas of reduced flexibility where the stiffer hinges are placed. Despite these localized effects, the global deformation behavior, including the rigid-body rotations of the Kagome lattice triangles, remains consistent with the reference solution.

5.5. Metamaterial structure with variable cross-sections

The performance of the metamaterial structure with a variable cross-section is investigated in this section. The analysis adopts the same initial conditions as described in Figs. 7(b) and 11, including the initial rotation of triangular elements by $\theta = 1.5°$. This setup aims to evaluate the influence of cross-sectional variation on the structural response. The numerical model consists of 132,600 DOF, using the same mesh pattern adopted for the converged model in Section 5.1. The results, depicted in Fig. 21, provide the σ vs. ϵ evolution for this configuration. The stress–strain curve highlights the impact of the variable cross-section on the mechanical behavior, showing distinct differences compared to the uniform cross-section case. The deformed configuration at $\epsilon = 0.05$ is also shown in Fig. 21, illustrating the global deformation behavior under significant strain.

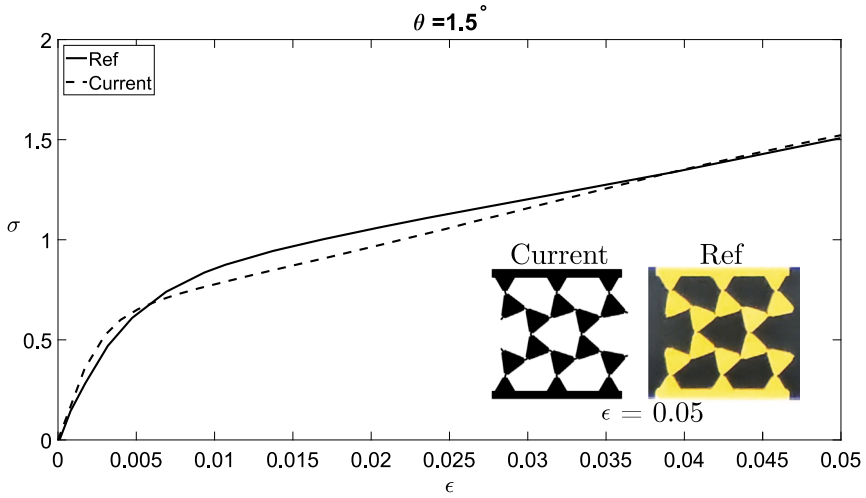

Fig. 12. Evolution of σ vs. ϵ for the metamaterial structure of Fig. 7(a) with an initial condition of triangles rotated by an angle $\theta = 1.5°$. Ref results are taken from Li et al. (2024). σ is calculated as the applied force F divided by the area over which the force is applied, while ϵ is determined as the ratio of the vertical displacement of the top plate to the initial structure height (67.60 mm).

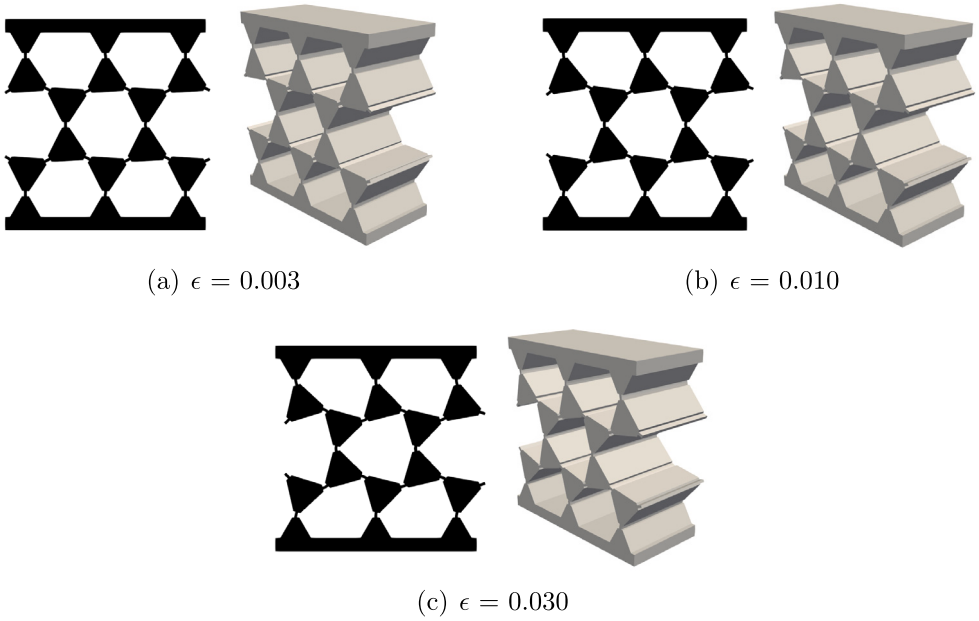

Fig. 13. Snapshots of the metamaterial structure of Fig. 7(a) with an initial condition of triangles rotated by an angle $\theta = 1.5°$. The cross-section view is taken at $y = 0$ mm.

Additionally, intermediate deformation stages are presented for $\epsilon = 0.003$, $\epsilon = 0.010$, and $\epsilon = 0.020$ in Figs. 22, 23, and 24, respectively. These snapshots provide a detailed view of the progressive deformation and highlight the distinct response characteristics of the variable cross-section design. This analysis underscores the potential of variable cross-section metamaterials in tailoring structural responses to specific performance requirements. The observed results suggest opportunities for optimizing the geometry to achieve desired mechanical properties, such as enhanced load distribution or deformation control. Fig. 25 illustrates the most advanced deformed configuration reached in this study, underscoring the method's remarkable capability to detect and represent deformations with high precision at any cross-section of the structure.

In Clip 1, only the inner triangles are shown, along with the corresponding displacements and rotations. Clip 2 depicts the same cross-section as in previous simulations, including all ten triangles, while Clip 3 presents the scenario where only the outer triangles are present. In each case, the deformation is reliably described, and additional parameters, such as strain, stress, or other mechanical fields, can be readily computed and visualized. This integrated approach not only provides a detailed deformation map but also enables the user to extract targeted performance metrics on demand. By seamlessly coupling geometric shape changes with mechanical response data, the methodology paves the way for fine-tuning the metamaterial's properties to meet specific design objectives. Moreover, rather than being confined to adjusting only the 2D cross-section, designers can exploit the full 3D parameter space. This broader design space facilitates the creation of custom-tailored structures with superior mechanical behavior.

6. Conclusions

This work presented a comprehensive numerical study of metamaterial structures based on the Kagome lattice mechanism, using the Carrera Unified Formulation (CUF) to achieve accurate and efficient modeling. The study explored the mechanical behavior of beam-like metamaterials, offering valuable insights into their deformation patterns.

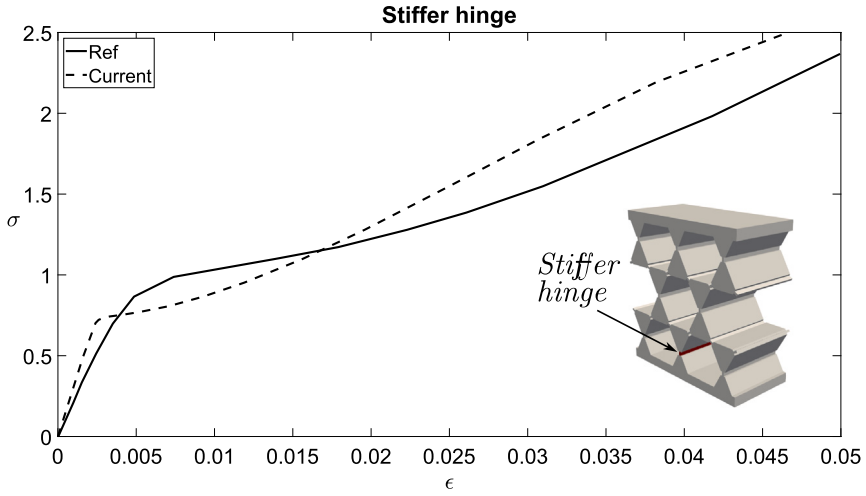

Fig. 14. σ vs. ϵ evolution for the metamaterial structure of Fig. 7(a) with a stiffer hinge. Ref results are taken from Li et al. (2024).

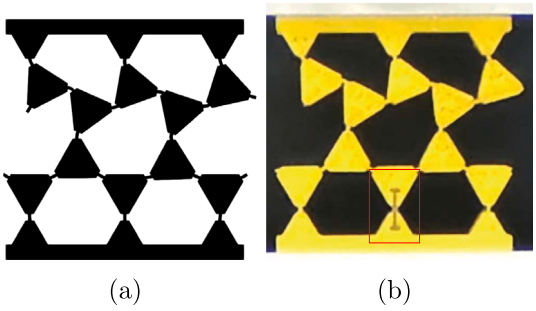

Fig. 15. Snapshots of the metamaterial structure of Fig. 7(a) with a stiffer hinge. Present study (a) vs. experimental results (b) taken from Li et al. (2024). σ is calculated as the applied force F divided by the area over which the force is applied, while ϵ is determined as the ratio of the vertical displacement of the top plate to the initial structure height (67.60 mm).

The key findings and contributions of this research are summarized as follows.

- The use of CUF enabled the development of enhanced 1D finite elements with 3D capabilities. This allowed for precise detection and prediction of deformations across the structure's cross-section, providing a robust framework for analyzing complex mechanical behaviors.
- The proposed model accurately captured both the buckling and post-buckling behaviors of the Kagome lattice structures. Deformed shapes were replicated with high fidelity, including rigid-body rotations of lattice triangles, highlighting the model's potential for applications requiring precise structural morphology and deformation control.
- The study demonstrated the versatility of Kagome lattice-based beam-like metamaterials in applications demanding controlled deformation and energy absorption. The introduction of stiffer hinges further showcased the ability to tailor mechanical responses, optimize load-carrying capacities, and adapt to specific design requirements.
- The results underscore the importance of localized stiffness modifications in enhancing the mechanical performance of metamaterials.
- Metamaterial structures based on the Kagome mechanism, featuring varying cross-sectional geometry across their width, can be easily modeled using CUF. This capability opens up possibilities for adapting the model to further investigate 3D Kagome lattices.

The findings of this study provide a robust foundation for future research into the design and optimization of metamaterial structures. One promising direction is the exploration of advanced material models, such as nonlinear material behaviors, to enhance the predictive accuracy of the numerical framework, particularly at higher strain levels. Hyperelastic materials have already been successfully included into the CUF framework (see Pagani and Carrera, 2023; Augello et al., 2023a; Pagani et al., 2024). Incorporating these advanced material models could provide a more comprehensive understanding of the material's response under complex loading conditions.

CRediT authorship contribution statement

R. Augello: Writing – original draft, Software, Methodology, Investigation, Data curation, Conceptualization. **E. Carrera:** Writing – review & editing, Supervision, Resources, Methodology, Data curation, Conceptualization. **W.Q. Chen:** Writing – review & editing, Validation, Supervision, Data curation. **B. Wu:** Writing – review & editing, Supervision. **Y.Z. Wang:** Writing – review & editing, Validation.

Declaration of competing interest

The authors declare that they have no known competing financial interests or personal relationships that could have appeared to influence the work reported in this paper.

Acknowledgments

This work is part of the project NOVITAS, funded by the European Union's Horizon Europe research and innovation program under the Marie Sklodowska-Curie grant agreement No 101059825.

The work was also supported by the National Natural Science Foundation of China (Nos. 12402107 and U24A2005).

Data availability

No data was used for the research described in the article.

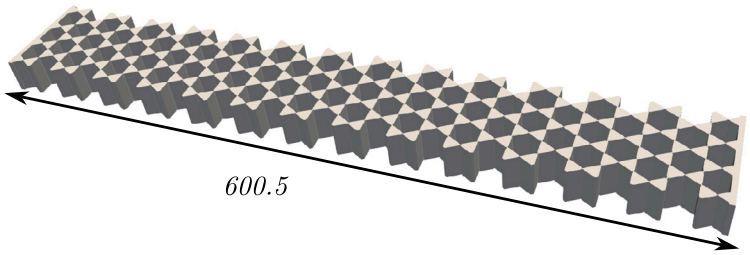

Fig. 16. Geometry of the beam-like metamaterial structure.

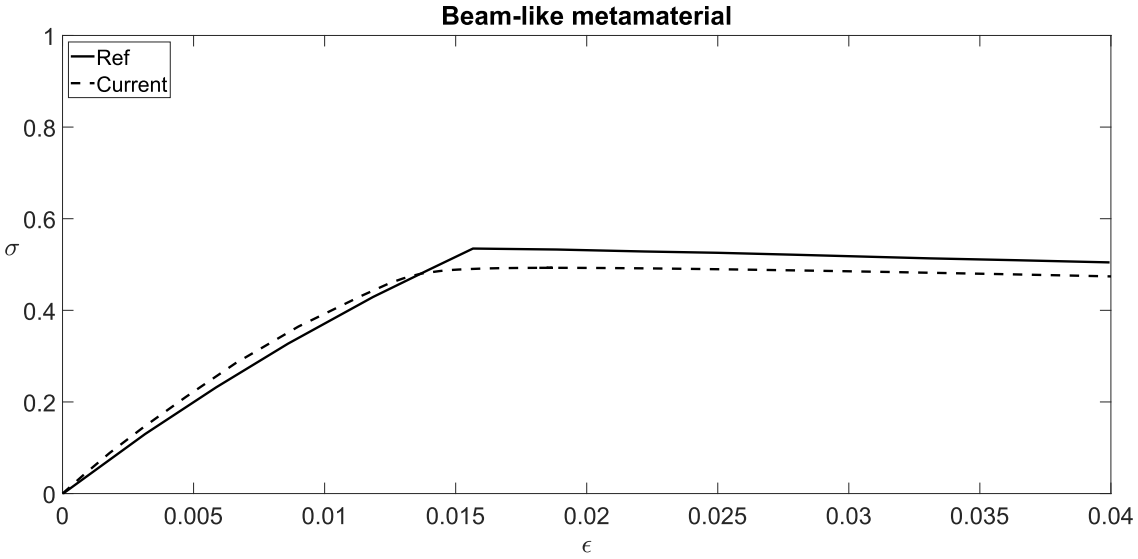

Fig. 17. Evolution of σ vs. ϵ for the beam-like metamaterial structure. Ref results are taken from Li et al. (2024). σ is calculated as the applied force F divided by the area over which the force is applied, while ϵ is determined as the ratio of the vertical displacement of the top plate to the initial structure height (67.60 mm).

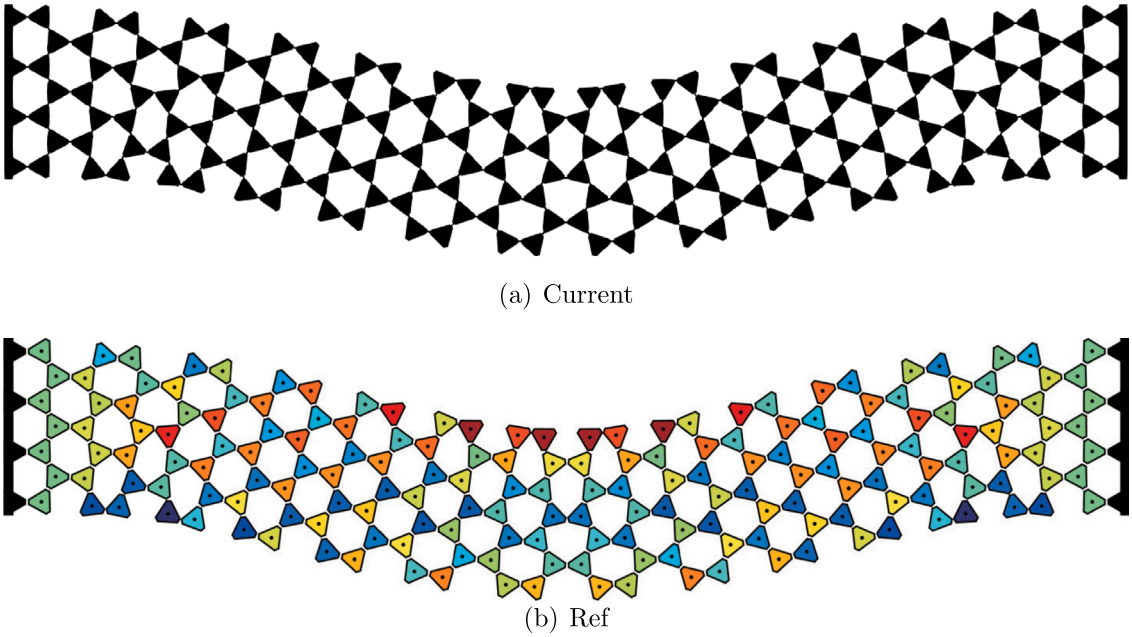

Fig. 18. Snapshots of the beam-like metamaterial structure shown in Fig. 7 for $\epsilon = 0.04$. Ref results are taken from Li et al. (2024).

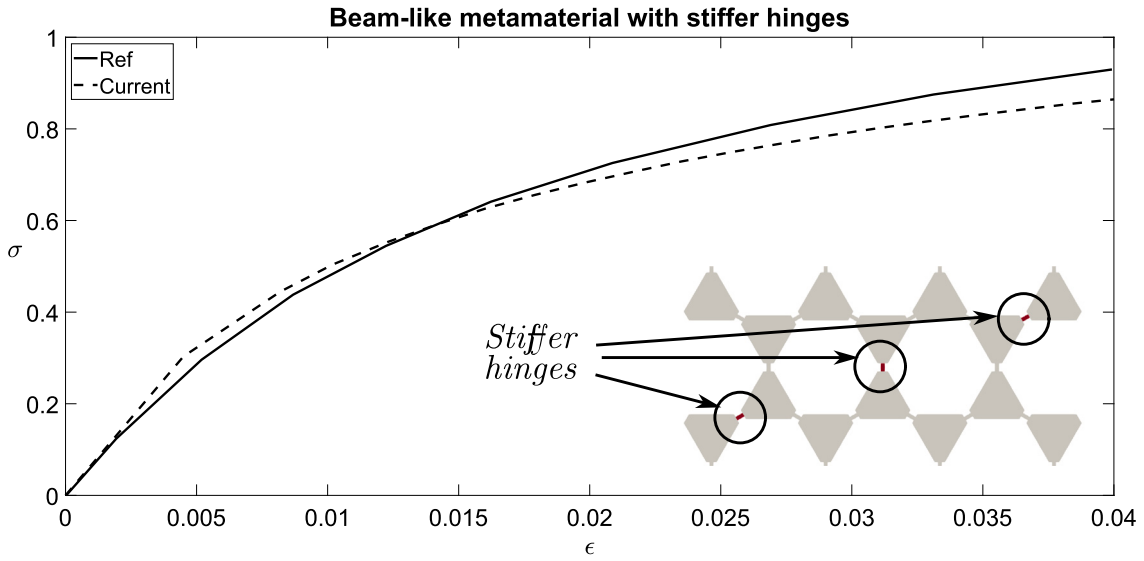

Fig. 19. Evolution of σ vs. ϵ for the beam-like metamaterial structure with stiffer hinges. Ref results are taken from Li et al. (2024).

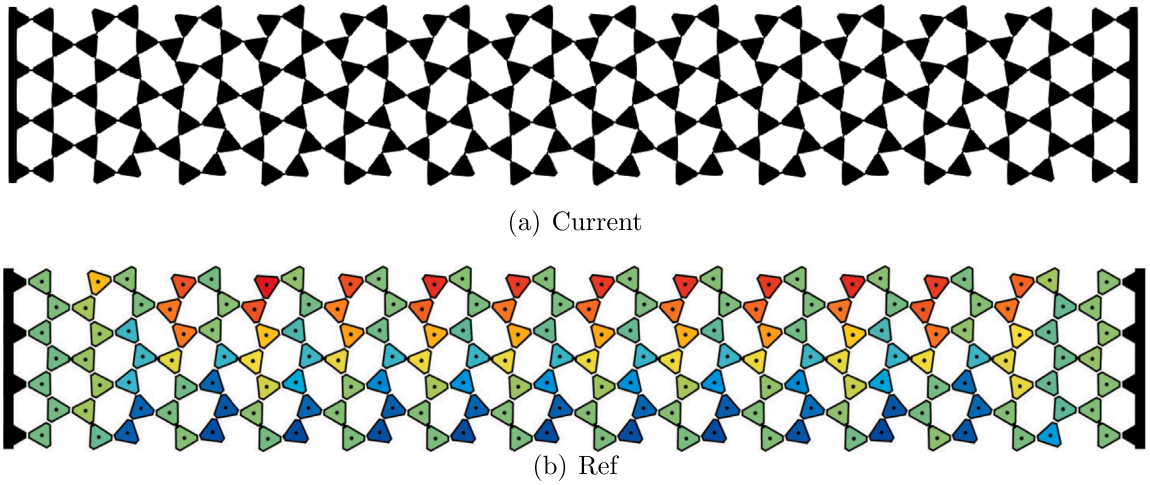

Fig. 20. Snapshots of the beam-like metamaterial structure with stiffer hinges from Fig. 7 for $\epsilon = 0.04$. Ref results are taken from Li et al. (2024). σ is calculated as the applied force F divided by the area over which the force is applied, while ϵ is determined as the ratio of the vertical displacement of the top plate to the initial structure height (67.60 mm).

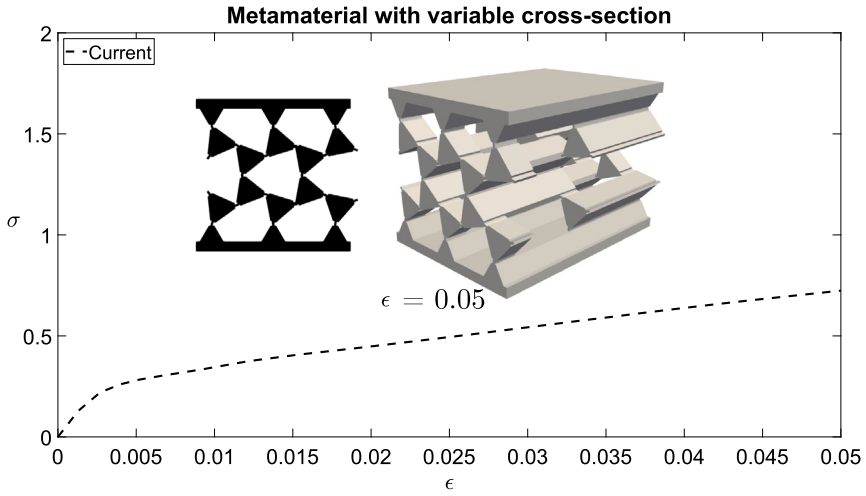

Fig. 21. Evolution of σ vs. ϵ for the metamaterial structure of Fig. 7(b). σ is calculated as the applied force F divided by the area over which the force is applied, while ϵ is determined as the ratio of the vertical displacement of the top plate to the initial structure height (67.60 mm).

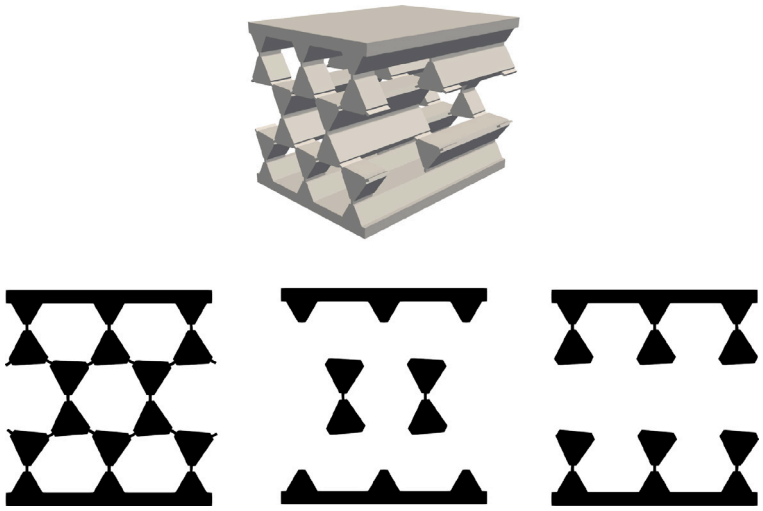

Fig. 22. Snapshots of the metamaterial structure of Fig. 7(b) for $\epsilon = 0.003$. Cross-section views are taken at $y = 0$ mm, $y = 20$ mm, and $y = 60$ mm.

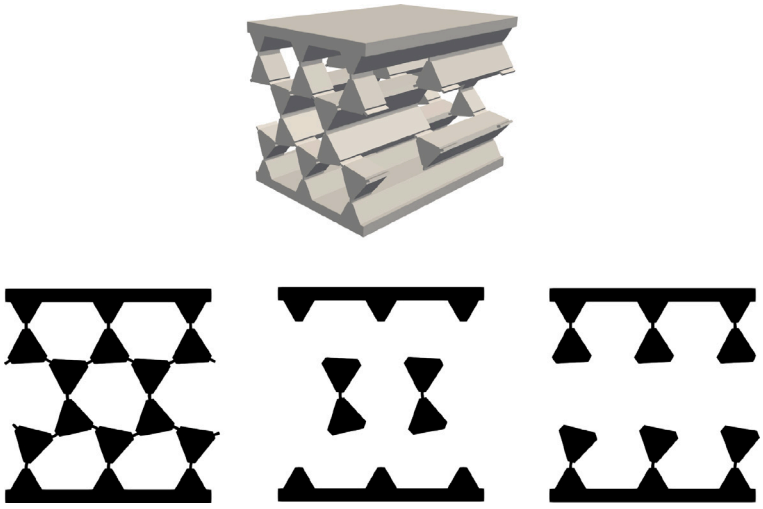

Fig. 23. Snapshots of the metamaterial structure of Fig. 7(b) for $\epsilon = 0.010$. Cross-section views are taken at $y = 0$ mm, $y = 20$ mm, and $y = 60$ mm.

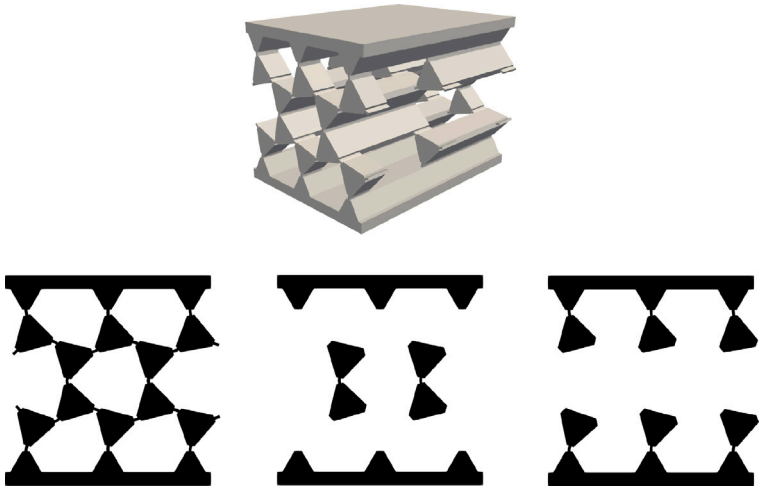

Fig. 24. Snapshots of the metamaterial structure of Fig. 7(b) for $\epsilon = 0.020$. Cross-section views are taken at $y = 0$ mm, $y = 20$ mm, and $y = 60$ mm.

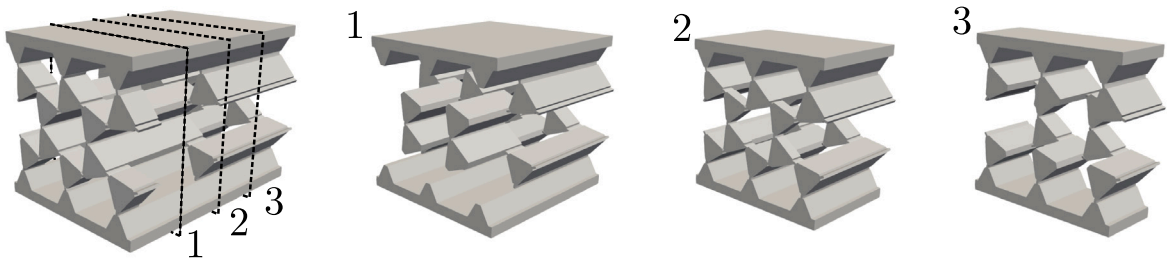

Fig. 25. Snapshots of the metamaterial structure of Fig. 7(b) for $\epsilon = 0.020$. Cross-section views are taken at $y = 0$ mm, $y = 20$ mm, and $y = 60$ mm.

References

Ablowitz, M.J., Cole, J.T., 2019. Topological insulators in longitudinally driven waveguides: Lieb and kagome lattices. Phys. Rev. A 99 (3), 033821.

Al Rifaie, M., Abdulhadi, H., Mian, A., 2022. Advances in mechanical metamaterials for vibration isolation: A review. Adv. Mech. Eng. 14 (3), 16878132221082872.

An, X., Sun, G., Yuan, X., Tian, Y., Hou, X., Fan, H., 2023a. Design of kagome lattice composite sandwich metastructures with high load bearing and low frequency vibration reduction properties. Compos. Part A: Appl. Sci. Manuf. 174, 107716.

An, X., Yuan, X., Fan, H., 2023b. Meta-Kagome lattice structures for broadband vibration isolation. Eng. Struct. 277, 115403.

Arabnejad, S., Pasini, D., 2013. Mechanical properties of lattice materials via asymptotic homogenization and comparison with alternative homogenization methods. Int. J. Mech. Sci. 77, 249–262.

Augello, R., Carrera, E., 2024. Nonlinear dynamics and band gap evolution of thin-walled metamaterial-like structures. J. Sound Vib. 578, 118329.

Augello, R., Carrera, E., Filippi, M., Pagani, A., Tortorelli, E., 2023a. Unified plate finite elements for the large strain analysis of hyperelastic material structures. Int. J. Non-Linear Mech. 155, 104465.

Augello, R., Pagani, A., Carrera, E., Pellegrino, S., 2023b. Folding simulation of TRAC longerons via unified one-dimensional finite elements. In: Aeronautics and Astronautics: AIDAA XXVII International Congress, vol. 37, Materials Research Forum LLC, p. 357.

Augello, R., Pellegrino, S., 2025. Vibration damping of thin-shell deployable structures through local buckling. In: AIAA SCITECH 2025 Forum. p. 0693.

Babaee, S., Shim, J., Weaver, J.C., Chen, E.R., Patel, N., Bertoldi, K., 2013. 3D soft metamaterials with negative Poisson's ratio. Adv. Mater. 25 (36), 5044–5049.

Bathe, K.-J., 2006. Finite element procedures. Klaus-Jurgen Bathe.

Bauer, J., Meza, L.R., Schaedler, T.A., Schwaiger, R., Zheng, X., Valdevit, L., 2017. Nanolattices: an emerging class of mechanical metamaterials. Adv. Mater. 29 (40), 1701850.

Carrera, E., 1994. A study on arc-length-type methods and their operation failures illustrated by a simple model. Comput. Struct. 50 (2), 217–229.

Carrera, E., Augello, R., Abu Salem, K., 2024. Evaluation of the effects of different materials on the dynamic properties of thin-walled metamaterial structures. Mech. Adv. Mater. Struct. 1–16.

Carrera, E., Cinefra, M., Petrolo, M., Zappino, E., 2014. Finite element analysis of structures through unified formulation. John Wiley & Sons.

Carrera, E., Giunta, G., Petrolo, M., 2011. Beam structures: classical and advanced theories. John Wiley & Sons, New York, USA.

Carrera, E., Pagani, A., 2016. Accurate response of wing structures to free-vibration, load factors, and nonstructural masses. AIAA J. 54 (1), 227–241.

Carrera, E., Pagani, A., Augello, R., 2018. Evaluation of geometrically nonlinear effects due to large cross-sectional deformations of compact and shell-like structures. Mech. Adv. Mater. Struct. 1–9.

Carrera, E., Pagani, A., Augello, R., 2021. Large deflection and post-buckling of thin-walled structures by finite elements with node-dependent kinematics. Acta Mech. 232 (2), 591–617.

Chen, Z., Guo, B., Yang, Y., Cheng, C., 2014. Metamaterials-based enhanced energy harvesting: A review. Phys. B 438, 1–8.

Chen, H., Nassar, H., Huang, G.L., 2018. A study of topological effects in 1D and 2D mechanical lattices. J. Mech. Phys. Solids 117, 22–36.

Cinefra, M., de Miguel, A.G., Filippi, M., Houriet, C., Pagani, A., Carrera, E., 2021. Homogenization and free-vibration analysis of elastic metamaterial plates by carrera unified formulation finite elements. Mech. Adv. Mater. Struct. 28 (5), 476–485.

Crisfield, M.A., 1981. A fast incremental/iterative solution procedure that handles "snap-through". In: Computational Methods in Nonlinear Structural and Solid Mechanics. Elsevier, Amsterdam, Netherlands.

Crisfield, M.A., 1983. An arc-length method including line searches and accelerations. Internat. J. Numer. Methods Engrg. 19 (9), 1269–1289.

Damanpack, A.R., Bodaghi, M., Liao, W.H., 2019. Experimentally validated multi-scale modeling of 3D printed hyper-elastic lattices. Int. J. Non-Linear Mech. 108, 87–110.

Filippi, M., Pagani, A., Carrera, E., 2018. Nonlinear dynamics of rotating structures and helicopter blades. In: ASME International Mechanical Engineering Congress and Exposition, vol. 52002, American Society of Mechanical Engineers, V001T03A037.

Hou, W., He, P., Yang, Y., Sang, L., 2023. Crashworthiness optimization of crash box with 3D-printed lattice structures. Int. J. Mech. Sci. 247, 108198.

Huang, L., Chowdhury, D.R., Ramani, S., Reiten, M.T., Luo, S.-N., Azad, A.K., Taylor, A.J., Chen, H.-T., 2012. Impact of resonator geometry and its coupling with ground plane on ultrathin metamaterial perfect absorbers. Appl. Phys. Lett. 101 (10).

Hughes, T.J.R., 2012. The finite element method: linear static and dynamic finite element analysis. Courier Corporation.

Li, J., Bao, R., Chen, W., 2024. Exploring static responses, mode transitions, and feasible tunability of kagome-based flexible mechanical metamaterials. J. Mech. Phys. Solids 186, 105599.

Li, X., Kohn, R.V., 2023. Some results on the Guest–Hutchinson modes and periodic mechanisms of the Kagome lattice metamaterial. J. Mech. Phys. Solids 178, 105311.

Lin, S., Cai, J., Xia, H., Ao, X., Liu, J., 2021. A reduced-order model based on finite element method for fast prediction of thermal performance of lattice structures. Int. Commun. Heat Mass Transfer 126, 105347.

Liu, Y., Zheng, G., Letov, N., Zhao, Y.F., 2021. A survey of modeling and optimization methods for multi-scale heterogeneous lattice structures. J. Mech. Des. 143 (4), 040803.

Maurin, F., Greco, F., Desmet, W., 2019. Isogeometric analysis for nonlinear planar pantographic lattice: discrete and continuum models. Contin. Mech. Thermodyn. 31, 1051–1064.

McBane, S., Choi, Y., 2021. Component-wise reduced order model lattice-type structure design. Comput. Methods Appl. Mech. Engrg. 381, 113813.

Nassar, H., Chen, H., Huang, G., 2020. Microtwist elasticity: A continuum approach to zero modes and topological polarization in kagome lattices. J. Mech. Phys. Solids 144, 104107.

Nelissen, W.E.D., Ayas, C., Tekõglu, C., 2019. 2D lattice material architectures for actuation. J. Mech. Phys. Solids 124, 83–101.

Nikolić, M., Karavelić, E., Ibrahimbegovic, A., Miš˘ cević, P., 2018. Lattice element models and their peculiarities. Arch. Comput. Methods Eng. 25, 753–784.

Pagani, A., Augello, R., Carrera, E., 2024. A high-order shell finite element for the large deformation analysis of soft material structures. Internat. J. Numer. Methods Engrg. 125 (7), e7417.

Pagani, A., Carrera, E., 2018. Unified formulation of geometrically nonlinear refined beam theories. Mechanics of Advanced Materials and Structures 25 (1), 15–31.

Pagani, A., Carrera, E., 2023. Unified one-dimensional finite element for the analysis of hyperelastic soft materials and structures. Mech. Adv. Mater. Struct. 30 (2), 342–355.

Pagani, A., Carrera, E., Augello, R., 2019. Evaluation of various geometrical nonlinearities in the response of beams and shells. AIAA J. 57 (8), 3524–3533.

Somnic, J., Jo, B.W., 2022. Status and challenges in homogenization methods for lattice materials. Materials 15 (2), 605.

Tankasala, H.C., Deshpande, V.S., Fleck, N.A., 2017. Tensile response of elastoplastic lattices at finite strain. J. Mech. Phys. Solids 109, 307–330.

Vigliotti, A., Pasini, D., 2012. Linear multiscale analysis and finite element validation of stretching and bending dominated lattice materials. Mech. Mater. 46, 57–68.

Vlădulescu, F., Constantinescu, D.M., 2020. Lattice structure optimization and homogenization through finite element analyses. Proc. Inst. Mech. Eng. Part L: J. Mater.: Des. Appl. 234 (12), 1490–1502.

Wang, Z., Lei, Z., Li, Z., Yuan, K., Wang, X., 2021. Mechanical reinforcement mechanism of a hierarchical kagome honeycomb. Thin-Walled Struct. 167, 108235.

Wang, Y., Wang, Z., Xia, Z., Poh, L.H., 2018. Structural design optimization using isogeometric analysis: a comprehensive review. Comput. Model. Eng. Sci. 117 (3), 455–507.

Wang, Y., Xu, H., Pasini, D., 2017. Multiscale isogeometric topology optimization for lattice materials. Comput. Methods Appl. Mech. Engrg. 316, 568–585.

Wu, Z.-J., Li, F.-M., Zhang, C., 2015. Vibration band-gap properties of three-dimensional kagome lattices using the spectral element method. J. Sound Vib. 341, 162–173.

Zhang, H.W., Wu, J.K., Fu, Z., 2010. Extended multiscale finite element method for elasto-plastic analysis of 2D periodic lattice truss materials. Comput. Mech. 45, 623–635.

Zienkiewicz, O.C., Taylor, R.L., 2005. The Finite Element Method for Solid and Structural Mechanics. Butterworth-Heinemann,Oxford, United Kingdom.